Realization of a three-dimensional quantum Hall effect in a Zeeman-induced second-order topological insulator on a torus

Zhe Hou,[1] Clara S. Weber,[2] Dante M. Kennes,[2,3] Daniel Loss,[1] Herbert Schoeller,[2] Jelena Klinovaja,[1] and Mikhail Pletyukhov[2,*]

[1]*Department of Physics, University of Basel, Klingelbergstrasse 82, CH-4056 Basel, Switzerland*

[2]*Institut für Theorie der Statistischen Physik, RWTH Aachen University, 52056 Aachen, Germany and JARA–Fundamentals of Future Information Technology, 52056 Aachen, Germany*

[3]*Max Planck Institute for the Structure and Dynamics of Matter, Center for Free Electron Laser Science, 22761 Hamburg, Germany*

(Received 20 December 2022; accepted 16 February 2023; published 27 February 2023)

We propose a realization of a quantum Hall effect (QHE) in a second-order topological insulator (SOTI) in three dimensions, which is mediated by hinge states on a torus surface. It results from the nontrivial interplay of the material structure, the Zeeman effect, and the surface curvature. In contrast to the conventional two-dimensional (2D)- and 3D-QHE, we show that the 3D-SOTI QHE is *not* affected by orbital effects of the applied magnetic field, and it exists in the presence of a Zeeman term only, induced, e.g., by magnetic doping. To explain the 3D-SOTI QHE, we analyze the boundary charge for a 3D-SOTI and establish its universal dependence on the Aharonov-Bohm flux threading through the torus hole. Exploiting the fundamental relation between the boundary charge and the Hall conductance, we demonstrate the universal quantization of the latter, as well as its stability against random disorder potentials and continuous deformations of the torus surface.

DOI: 10.1103/PhysRevB.107.075437

I. INTRODUCTION

The quantum Hall effect (QHE), observed by Klitzing *et al.* [1] in 1980, is one of the fundamental phenomena in condensed-matter physics. It has since become a driving force for the field of topological insulators (TIs) with a plethora of new topological materials discovered in the past few decades [2–7]. As a consequence, many intriguing generalizations, such as the anomalous QHE (in the absence of an external magnetic field) in two dimensions [8–22] and the three-dimensional (3D)-QHE [23–27] have been studied. Moreover, the concept of TIs has been extended to higher-order TIs, which are governed by a new bulk-boundary correspondence [28–35]. For example, a second-order (third-order) TI with dimension D features $D-2$ ($D-3$) -dimensional hinge (corner) states. Recently, within 3D second-order TIs (3D-SOTIs), an additional class of systems exhibiting the QHE has been proposed [31,36–39].

One way to realize a 3D-SOTI is to build on a 3D-TI [6,7,12,40–42] and introduce anisotropic gaps on different surfaces (boundaries), e.g., with an effective Zeeman term by magnetic doping or using an external magnetic field [38,39,43–49]. At special positions where the effective gap closes and reverses sign, topological hinge or corner states emerge, in analogy to the Jackiw-Rebbi mode [50].

In this paper, we will consider such a model and discuss a specific realization using a torus geometry (or smooth deformations thereof) as shown in Fig. 1, where the emerging hinge states are shown with blue and red arrows. This geometry allows us to insert a magnetic flux ϕ through the torus hole, and thus we construct a 3D analog of the Corbino disk, which is used in the Laughlin argument for the conventional 2D-QHE [51]. However, in contrast to the Corbino setup, the 3D-SOTI QHE discussed here is *not* induced by orbital effects but results purely from the Zeeman effect.

While there are several approaches known to deduce the conventional 2D quantized Hall conductance [51–54], we will present a generalization of a recently developed boundary charge approach to the case of a 3D-SOTI, which, most importantly, is applicable to *both* clean and disordered systems. It is based on recent detailed studies of the boundary charge in one-dimensional (1D) modulated wires [55–65], together with dimensional extensions to 2D-QHE models [56,57] revealing the fundamental relationship between the linear dependence of the boundary charge on the phase of the potential in 1D models and the quantized Hall conductance in 2D models, a concept that can even be generalized to explain the fractional QHE in the presence of interactions [62].

Most importantly, we demonstrate for the 3D-SOTI model on a torus that the boundary charge, driven by the Aharonov-Bohm flux $\phi = f\phi_0$, where ϕ_0 is the flux quantum, shows a linear relation with respect to f, with the slope being universal and quantized to integer numbers $\pm e$, where e is the electron charge. Examining all states below the chemical potential, we reach a remarkable conclusion: the whole contribution to the boundary charge comes only from the topmost occupied valence band [shown in orange in Fig. 2(a)]. We further include disorder effects by considering a 3D tight-binding (tb) counterpart of our continuum model with broken rotational symmetry and show the robustness of the quantized slope. The boundary charge concept thus provides a powerful tool

*pletmikh@physik.rwth-aachen.de

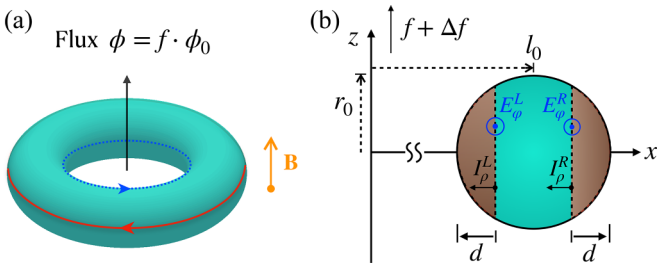

FIG. 1. (a) Torus model and (b) its 2D cross-section in the x-z plane. The torus hole is pierced by the Aharonov-Bohm flux $\phi = f\phi_0$. In addition, there is a constant uniform magnetic field $\mathbf{B}$ in the z direction. The system hosts the clockwise (red) and counterclockwise (blue) propagating hinge modes at the outer and inner equatorial rings of the torus, respectively. The hinge states are localized within the outer (or right) and the inner (or left) boundary regions [shown in brown in (b)] of the width d (as measured in the radial direction). The electric fields $E_\varphi^{R,L}$ and the Hall currents $I_\rho^{R,L}$ are generated upon changing f as shown in (b).

in characterizing 3D-SOTIs, and it universally explains topological effects in condensed-matter systems as well as their stability against random potential disorder and continuous surface deformations.

II. MODEL

We consider a continuum model in a finite three-dimensional region, which is confined to the interior of a torus [see Fig. 1(a)], to realize a second-order TI with a minimal set of ingredients, given by band inversion, spin-orbit coupling, magnetic flux, and the Zeeman term. The Hamiltonian (with $e = \hbar = 1$) is given by

$$H = \sigma_z \left[\frac{(\mathbf{p} + \mathbf{A})^2}{2m^*} - \delta \right] + \alpha\, \sigma_x (\mathbf{p} + \mathbf{A}) \cdot \mathbf{s} + \varepsilon_Z s_z, \qquad (1)$$

where $\mathbf{p}$ and $\mathbf{S} = \frac{1}{2}\mathbf{s}$ are 3D vectors of the momentum and the physical spin-$\frac{1}{2}$ operators, respectively. The parameters m^* and $\alpha > 0$ are the effective mass of the electron and the spin-orbit interaction, respectively, while ε_Z denotes the Zeeman energy. Both the magnetization direction inducing the Zeeman term and the uniform magnetic field $\mathbf{B}$ generated by the vector potential $\mathbf{A}$ are assumed to point along the z-axis. We note that ε_Z is an independent parameter, controllable by magnetic doping. The Pauli matrices σ_i span the orbital degrees of freedom. The parameter $\delta > 0$ is chosen positive in order to realize the band inversion at finite values of α, ε_Z, and $B \equiv |\mathbf{B}|$. The vector potential $\mathbf{A} = \mathbf{A}_B + \mathbf{A}_\phi = \frac{B\rho}{2}\mathbf{e}_\varphi + \frac{\phi}{2\pi\rho}\mathbf{e}_\varphi \equiv \frac{B\rho}{2}\mathbf{e}_\varphi + \frac{f}{\rho}\mathbf{e}_\varphi$ contains the terms generating both the uniform magnetic field B and the Aharonov-Bohm (AB) magnetic flux ϕ. Here, we used the cylindrical coordinates (ρ, φ, z) and introduced the number of flux quanta $f = \frac{\phi}{\phi_0} \overset{!}{=} \frac{\phi}{2\pi}$.

Besides the spin-orbit length $l_{\rm so} = 1/(\alpha m^*)$, we introduce two further typical scales l_B and l_Z associated with the orbital magnetic field and the Zeeman term, respectively, via $B = 1/l_B^2$ and $\varepsilon_Z = 1/(2m^* l_Z^2)$. In the main part of the paper, we discuss the most critical case $l_B \sim l_Z$ of strong orbital fields, and we show that the Hall conductance is quantized.

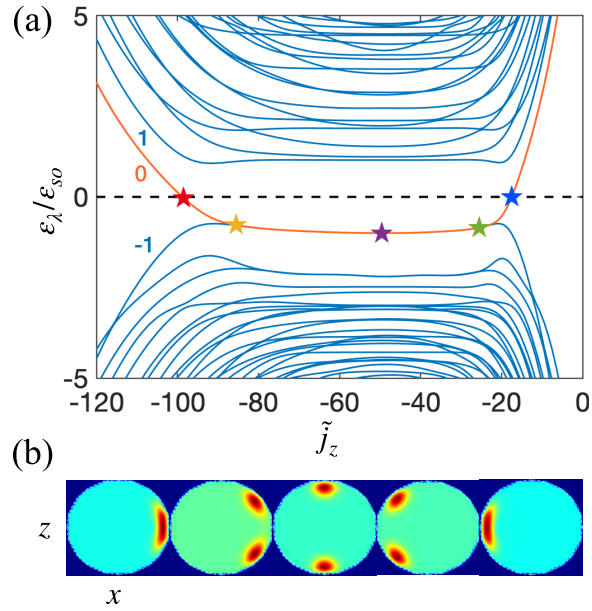

FIG. 2. (a) Low-energy spectrum of torus model in units of spin-orbit energy $\varepsilon_{\rm so} = \frac{m^*\alpha^2}{2}$. Band indices are $\lambda \leqslant -1$ for valence bands, $\lambda \geqslant 1$ for conduction bands, and $\lambda = 0$ for the band hosting Landau surface states in the plateau region together with the right (R) and left (L) hinge states in the steep parts of the dispersion. The parameters are $\delta = 3\,\varepsilon_{\rm so}$, $l_B = l_Z = l_{\rm so}$, $l_0 = 10\,l_{\rm so}$, and $r_0 = 5\,l_{\rm so}$. The lattice constant was chosen $a = l_{\rm so}/5$ in the tb model calculation. The black dashed line denotes the chemical potential $\mu = 0$. Note that the two bands $\lambda = 0, -1$ are almost degenerate along the plateau region but separated by an (invisible) small gap. (b) Probability density of the five states labeled with star symbols in (a) on the band $\lambda = 0$ at $\tilde{j}_z = -98.5, -85.5, -49.5, -25.5, -17.5$, shown from left to right in the same sequence as in (a). The red (blue) star denotes the R (L) hinge state, while the yellow, purple, and green stars denote the Landau surface states with the intermediate angular positions of the density localization.

In the torus geometry and in the absence of disorder, the model (1) possesses axial symmetry generated by the z-component of the total angular momentum operator $J_z = L_z + \frac{1}{2}s_z = -i\frac{\partial}{\partial\varphi} + \frac{1}{2}s_z$. Exploiting this symmetry, we reduce the 3D model to an effective 2D model with the Hamiltonian (see Appendix A for details)

$$h_{2D} = \frac{\sigma_z}{2m^*}\left[-\frac{\partial^2}{\partial x^2} + \frac{J^2(x)}{x^2} - s_z\frac{J(x)}{x^2} - \frac{\partial^2}{\partial z^2} - 2m^*\delta \right] + \alpha\sigma_x\left[-is_x\frac{\partial}{\partial x} + s_y\frac{J(x)}{x} - is_z\frac{\partial}{\partial z} \right] + \varepsilon_Z s_z. \qquad (2)$$

It is defined on the disk of radius r_0 in the $(x > 0, z)$ half-plane, which is displaced away from the z-axis by $l_0 > r_0$ [see Fig. 1(b)]. We introduce the following continuous parameter $\tilde{j}_z = j_z + f$, where j_z are half-integer eigenvalues of the operator J_z, and f is restricted to fractional values, $f \in [0, 1)$, interpolating between adjacent values of j_z. The parameter $\tilde{j}_z$ appears inside the function $J(x) = \tilde{j}_z + \frac{Bx^2}{2}$, where the last term accounts for the orbital B-field effect.

III. HINGE STATES

Approximating (2) by its tight-binding (tb) lattice counterpart or by solving it directly in an appropriately chosen basis (see in Appendix A), we calculate the band structure shown in Fig. 2(a). Between the valence $[\varepsilon_{\lambda\leqslant -1}(\tilde{j}_z) < \mu]$ and conduction $[\varepsilon_{\lambda\geqslant 1}(\tilde{j}_z) > \mu]$ bands, there is a distinguished band $\varepsilon_{\lambda=0}(\tilde{j}_z)$ (orange line) that crosses the chemical potential $\mu = 0$ at the two points $\tilde{j}^*_{z;R,L}$ [with $\varepsilon_0'(\tilde{j}^*_{z;R,L}) \lessgtr 0$].

As shown in Fig. 2(b), the states on the negative (positive) linear slope near $\tilde{j}^*_{z,R}$ ($\tilde{j}^*_{z,L}$) [indicated by the red (blue) star] form the right (left) [or R (L)] hinge mode, with the density localized near the disk's right (left) side $\theta = \frac{\pi}{2}$ ($\theta = -\frac{\pi}{2}$) [here we use the polar coordinates associated with the disk $x = l_0 + r\sin\theta$, $z = r\cos\theta$, with $\theta \in (-\pi, \pi]$ and $r < r_0$]. The R (L) hinge mode propagates in the clockwise (counterclockwise) direction along the outer (inner) equator of the torus (looking from the top); see the red (blue) line in Fig. 1(a). To reveal details of the hinge mode properties, including their spinor structure, we rely on the low-energy theory (see Appendix A) valid in the regime $l_0 \gg r_0 \gg l_{\rm so}$ and $\frac{r_0}{l_{\rm so}} \gg \frac{l_{\rm so}^2}{l_Z^2} \gg \frac{l_{\rm so}}{r_0}$.

It turns out that the R (L) hinge mode is exponentially localized near the torus surface on the scale $l_{\rm so}$. Its angular localization is Gaussian, with the variance $\sigma_\theta^{\rm hinge} = \frac{l_Z}{\sqrt{r_0 l_{\rm so}/2}} \gg \frac{l_{\rm so}}{r_0}$ featuring the scale l_Z, which is indicative of the Zeeman mechanism of the mode's stabilization. The energy dispersions are approximated by $\varepsilon_0^{R,L}(\tilde{j}_z) \approx \mp\frac{\alpha}{l_0}(\tilde{j}_z - \tilde{j}^*_{z;R,L})$, where the offsets $\tilde{j}^*_{z;R,L} \approx -\frac{B\cdot\pi(l_0\pm r_0)^2}{2\pi}$ account the orbital B-field effects—its flux quanta through the torus' outer/inner equatorial rings.

IV. PLATEAU REGION

In the broad range $\tilde{j}^*_{z,R} < \tilde{j}_z < \tilde{j}^*_{z,L}$, there is a nearly degenerate plateau of weakly dispersing Landau surface states (LSSs) [between yellow and green stars in Fig. 2(a)], which are also localized near the torus surface on the scale $l_{\rm so}$. Looking first at the states in the plateau's middle [that is, near the purple star in Fig. 2(a) at $\tilde{j}_z \approx -\frac{B\pi l_0^2}{2\pi}$], we observe that they are the linear combinations of the so-called top and bottom LSSs localized near $\theta = 0$ and $\theta = \pi$, respectively. Due to the finite torus size, the splitting between ε_0 and ε_{-1} in the plateau's middle is estimated by an exponentially small value $\propto\alpha\sqrt{B}e^{-2Br_0^2}$ (for details, see Appendix A). The density of the higher-energy state, i.e., belonging to the band ε_0, is shown in the central inset of Fig. 2(b). This state is drastically different from the above-discussed hinge states, since its stabilization occurs due to the orbital B-field effect, while the Zeeman term produces only a perturbative contribution $-\varepsilon_Z$ to its energy. We also find that its angular variance $\sigma_\theta^{\rm LSS} = \frac{l_B}{r_0}$ is both independent of ε_Z and smaller than $\sigma_\theta^{\rm hinge}$.

The other states belonging to ε_0 connect the top-bottom LSSs in the plateau's middle with the R (L) hinge mode. The density localization position of the intermediate states evolves in the θ direction with altering $\tilde{j}_z$ [see Fig. 2(b)], while the variance σ_θ increases from $\sigma_\theta^{\rm LSS}$ to $\sigma_\theta^{\rm hinge}$. Their stabilization mechanism accordingly changes from the orbital to the Zeeman effect.

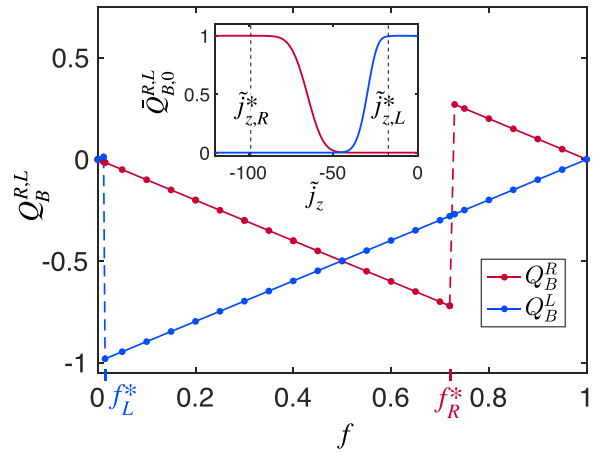

FIG. 3. Boundary charges vs f. The width of the boundary region is $d = 3\,l_{\rm so}$, other parameters being the same as in Fig. 2. Numerical j_z-summation spans the wide enough range $[-199.5, 100.5]$ ensuring convergence. The slope for the right (left) boundary charge is -0.9993 (0.9952), which is obtained by linear fitting of the longer segment of each curve (we use a discrete spacing $\Delta f = 0.05$ refining it to $\Delta f = 0.01$ near the jump positions). The slope values agree with the corresponding jump sizes. The latter occur at the flux values $f_R^* \approx 0.72$ and $f_L^* \approx 0.01$, when an electron enters or leaves the system. Inset: Partial contributions $\bar{Q}_{B,0}^{R,L}(\tilde{j}_z)$ from the band $\varepsilon_0(\tilde{j}_z)$ and the summation constraints imposed by the roots $\tilde{j}^*_{z,R} \approx -98.78$ and $\tilde{j}^*_{z,L} \approx -17.49$ of the equation $\varepsilon_0(\tilde{j}_z) = \mu = 0$. Note that $\tilde{j}^*_{z,R} - f_R^* = -99.5$ and $\tilde{j}^*_{z,L} - f_L^* = -17.5$ are half-integers.

V. BOUNDARY CHARGE AND 3D-SOTI QHE

A convenient way to introduce the Hall conductance is to define it via the charge localized within an appropriately chosen boundary region [55–58]. In our model, the outer (R) and the inner (L) boundary regions $\mathcal{B}_{R,L}$ [shown in brown in Fig. 1(b)] are bounded by the cylindrical shells of the radii $\rho_{R,L} = l_0 \pm (r_0 - d)$, respectively. Choosing the width d such that $r_0 \gg d \gg l_{\rm so}$, $\frac{l_Z^2}{l_{\rm so}}$, we ensure that the R/L hinge states are fully confined within $\mathcal{B}_{R,L}$, respectively. It is natural to define the boundary charges $Q_B^{R,L}(f) = \sum_\lambda Q_{B,\lambda}^{R,L}(f)$, with

$$Q_{B,\lambda}^{R,L}(f) = \sum_{j_z,\varepsilon_\lambda(\tilde{j}_z)<\mu} \bar{Q}_{B,\lambda}^{R,L}(\tilde{j}_z) - \sum_{j_z,\varepsilon_\lambda(j_z)<\mu} \bar{Q}_{B,\lambda}^{R,L}(j_z), \qquad (3)$$

where $\bar{Q}_{B,\lambda}^{R,L}(\tilde{j}_z) = \int_{\mathcal{B}_{R,L}} dx\,dz|\Psi_\lambda(x,z;\tilde{j}_z)|^2$ is a partial contribution of the state (λ, j_z) evaluated at the AB flux $f\phi_0$. To make the definition (3) insensitive to a specific choice of d, we subtract a large background contribution at $f = 0$ (the second term).

The central result of this paper, supported by the numerical result shown in Fig. 3, is that the flux dependence $Q_B^{R,L}(f)$ is piecewise linear,

$$Q_B^{R,L}(f) = \mp f \pm \Theta(f - f_{R,L}^*), \qquad (4)$$

with jumps at $f = f_{R,L}^*$, where $\tilde{j}^*_{z;R,L} - f$ is a half-integer. The slope value is correlated with the jump size such that the periodicity $Q_B^{R,L}(f) = Q_B^{R,L}(f+1)$ is maintained. Changing the flux adiabatically in time, the immediate consequence of (4) is the quantization of the Hall conductance, relating the Hall

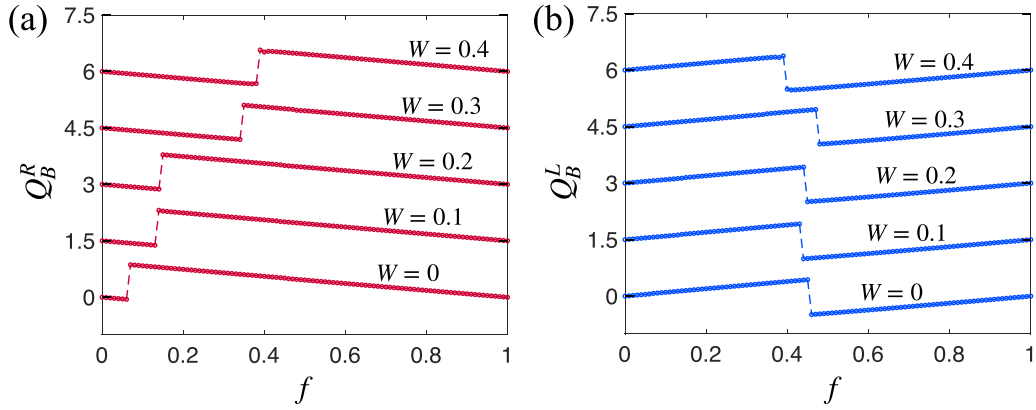

FIG. 4. Boundary charges vs f calculated (with spacing $\Delta f = 0.01$) for the 3D tb model in the presence of disorder potentials uniformly distributed on the interval $[-W/2, W/2]$ (we consider a single random disorder configuration for each disorder strength W; other parameters are as in Fig. 2). The results for every next W (in units of $\varepsilon_{\rm so}$) are shifted vertically with the step 1.5. The fitted slope value for the right (left) boundary charge is -0.915 (0.914); these values are the same for each W up to the quoted accuracy. Small deviations from the universal values ∓ 1 occur due to the larger lattice constant $a_{\rm 3D} = l_{\rm so}$ used in the 3D calculations (for further details, see Appendix C).

current to the electric field via $I_\rho^{R,L} = \sigma_{\rho\varphi}^{R,L} E_\varphi^{R,L}$; see Fig. 1(b) and the discussion in Refs. [56,57,62]. Using Faraday's law and the continuity equation, we get $E_\varphi^{R,L} = -\dot{\phi}/(2\pi\rho_{R,L})$ and $I_\rho^{R,L} = \pm\dot{Q}_B^{R,L}/(2\pi\rho_{R,L})$. Together with $\dot{Q}_B^{R,L} \approx \frac{\partial Q_B^{R,L}}{\partial f}\dot{f}$ and $\dot{\phi} = 2\pi\dot{f}$, we obtain the Hall conductance quantization $\sigma_{\rho\varphi}^{R,L} = \frac{1}{2\pi} \stackrel{!}{=} \frac{e^2}{h}$, which holds away from $f = f_{R,L}^*$.

The second important result is that the contribution $Q_{B,\lambda}^{R,L}$ from all valence bands with $\lambda \leqslant -1$ is negligible (see Appendix B for the numerical verification). This is an intuitively expected result, since the valence band ε_{-1} is separated from the band ε_0 by the topologically trivial, though exponentially small, gap. The nonzero contribution to the boundary charge is thus provided by ε_0, which is shown in the inset of Fig. 3.

Let us provide the analytical arguments explaining the above results. The discrete jumps of $Q_B^{R,L}(f)$ at $f = f_{R,L}^*$ obviously occur at those flux values for which a half-integer j_z exists with $j_z + f_{R,L}^* = \tilde{j}_{z;R,L}^*$. These are the points where the R/L hinge modes of the $\lambda = 0$ band cross the chemical potential, leading to a jump of $Q_{B,\lambda=0}^{R,L}(f)$ by ± 1. In contrast, for all fully occupied bands $\lambda < 0$, there is no jump.

The linear dependence on the flux follows essentially from the smooth behavior of $\bar{Q}_{B,\lambda}^{R,L}(\tilde{j}_z)$ as a function of $\tilde{j}_z$, i.e., it varies typically on the scale $\Delta\tilde{j}_z \sim \tilde{j}_{z,L}^* - \tilde{j}_{z,R}^*$ of the plateau size; see the inset in Fig. 3 for $\lambda = 0$ [the same applies for all $\lambda \neq 0$, except that the asymptotic values of $\bar{Q}_{B,\lambda}^{R,L}(\tilde{j}_z)$ at $\tilde{j}_z \to \pm\infty$ are coinciding]. The plateau size is estimated by the number $N_B \sim r_0 l_0 / l_B^2$ of the B-field flux quanta threaded through the torus surface. Therefore, the nth derivative of $\bar{Q}_{B,\lambda}^{R,L}(\tilde{j}_z)$ scales like $1/N_B^n$ in the plateau's region, being negligibly small outside it. Along with an additional factor N_B from the sum over j_z, this scaling leads to the scaling $(\frac{d}{df})^n Q_{B,\lambda}^{R,L}(f) \sim 1/N_B^{n-1}$. Thus, all higher-order ($n \geqslant 2$) derivatives are negligible at $N_B \gg 1$. This can be achieved to any desired accuracy by increasing the scale l_0. Therefore, only the linear term in f contributes significantly to $Q_{B,\lambda}^{R,L}(f)$ for each band. Since the slope value of the linear term of $Q_{B,\lambda}^{R,L}(f)$ is correlated with the discrete jumps due to the periodicity property $Q_{B,\lambda}^{R,L}(f) = Q_{B,\lambda}^{R,L}(f+1)$, we find that the slope is zero for all bands $\lambda < 0$, and ∓ 1 for $\lambda = 0$. This proves the negligible contribution of the valence bands $\varepsilon_{\lambda\leqslant -1}$ and the entire contribution of the band ε_0 to the universal linear slope of the total boundary charge.

VI. DISORDER EFFECTS

We add random disorder potentials to every site of the 3D tb lattice realization of the Hamiltonian (1). Disorder breaks the rotational symmetry, and neither the quantum number j_z nor the band index λ remains well-defined. Remarkably, the boundary charge $Q_B^{R,L}$, in which all the states below μ are accounted for, as well as its relation to the Hall conductance are still well-defined. In Fig. 4 we show (providing the details of the calculation in Appendix C) that the linear slopes of $Q_B^{R,L}(f)$ remain very close to the universal values ∓ 1, i.e., staying essentially unaffected by disorder (the latter affects only the jump position, which is nonuniversal). This demonstrates the fundamental significance of the boundary charge concept: It is capable of explaining the Hall conductance quantization even in the disordered case, when the simple clean-case explanation presented above is no longer applicable.

VII. DISCUSSION

The proposed 3D-SOTI QHE is robust to disorder, which is very promising for its experimental realization using standard 3D-TIs with Zeeman fields induced by external magnetic fields, magnetic doping, or nearby ferromagnets. It occurs specifically only in 3D systems (for system sizes exceeding the localization length of hinge states) and is insensitive to orbital effects (see Appendix D), providing various fingerprints for its unique observation. Moreover, it is robust to shape distortions and will even occur in a spherical model with an infinitesimally thin hollow tube along the vertical axis (to allow for the Aharonov-Bohm flux insertion): The boundary

charge showcases the same qualitative features as in the torus model (see Appendix E), and its detailed study opens another avenue of future research.

ACKNOWLEDGMENTS

This work was supported by the Deutsche Forschungsgemeinschaft via RTG 1995, the Swiss National Science Foundation (SNSF), and by the Deutsche Forschungsgemeinschaft (DFG, German Research Foundation) under Germany's Excellence Strategy—Cluster of Excellence Matter and Light for Quantum Computing (ML4Q) EXC 2004/1-390534769. We acknowledge support from the Max Planck–New York City Center for Non-Equilibrium Quantum Phenomena. Simulations were performed with computing resources granted by RWTH Aachen University under projects rwth0752 and rwth0841, and at sciCORE [66] scientific computing center at University of Basel. Funding was received from the European Union's Horizon 2020 research and innovation program (ERC Starting Grant, Grant Agreement No. 757725).

APPENDIX A: EFFECTIVE LOW-ENERGY THEORY

1. Derivation of the effective two-dimensional model by exploiting the rotational symmetry

In the cylindrical coordinates (ρ, φ, z), the Hamiltonian (1) acquires the form

$$H = \frac{\sigma_z}{2m^*}\Big[-\frac{1}{\rho}\frac{\partial}{\partial\rho}\rho\frac{\partial}{\partial\rho} + \frac{1}{\rho^2}\Big(-i\frac{\partial}{\partial\varphi} + f + \frac{B\rho^2}{2}\Big)^2 - \frac{\partial^2}{\partial z^2} - 2m^*\delta\Big] + \alpha\sigma_x\Big[-is_\rho\frac{\partial}{\partial\rho} + \frac{s_\varphi}{\rho}\Big(-i\frac{\partial}{\partial\varphi} + f + \frac{B\rho^2}{2}\Big) - is_z\frac{\partial}{\partial z}\Big] + \varepsilon_Z s_z, \tag{A1}$$

where

$$s_\rho = s_x\cos\varphi + s_y\sin\varphi, \tag{A2}$$

$$s_\varphi = -s_x\sin\varphi + s_y\cos\varphi. \tag{A3}$$

Performing the unitary transformation $U_\varphi = e^{-\frac{i}{2}\varphi}e^{\frac{i}{2}s_z\varphi}$, which transforms

$$U_\varphi s_\rho U_\varphi^\dagger = s_x, \tag{A4}$$

$$U_\varphi s_\varphi U_\varphi^\dagger = s_y, \tag{A5}$$

and

$$U_\varphi J_z U_\varphi^\dagger = U_\varphi\Big(-i\frac{\partial}{\partial\varphi} + \frac{1}{2}s_z\Big)U_\varphi^\dagger = -i\frac{\partial}{\partial\varphi} + \frac{1}{2} \equiv \hat{J}_z, \tag{A6}$$

supporting the periodic boundary conditions in φ, we obtain

$$h_{3D} = U_\varphi H U_\varphi^\dagger = \frac{\sigma_z}{2m^*}\Big[-\frac{1}{\rho}\frac{\partial}{\partial\rho}\rho\frac{\partial}{\partial\rho} + \frac{1}{\rho^2}\Big(\hat{J}_z - \frac{1}{2}s_z + f + \frac{B\rho^2}{2}\Big)^2 - \frac{\partial^2}{\partial z^2} - 2m^*\delta\Big] + \alpha\sigma_x\Big[-is_z\frac{\partial}{\partial\rho} + \frac{s_y}{\rho}\Big(\hat{J}_z - \frac{1}{2}s_z + f + \frac{B\rho^2}{2}\Big) - is_z\frac{\partial}{\partial z}\Big] + \varepsilon_Z s_z. \tag{A7}$$

$$+ \alpha\sigma_x\Big[-is_z\frac{\partial}{\partial\rho} + \frac{s_y}{\rho}\Big(\hat{J}_z - \frac{1}{2}s_z + f + \frac{B\rho^2}{2}\Big) - is_z\frac{\partial}{\partial z}\Big] + \varepsilon_Z s_z. \tag{A8}$$

By virtue of the U_φ transformation, we remove the φ-dependence from the Hamiltonian and thereby explicitly manifest the rotational symmetry about the z axis, $[h_{3D}, \hat{J}_z] = U_\varphi[H, J_z]U_\varphi^\dagger = 0$.

The total angular momentum operator $\hat{J}_z$ can be replaced by its half-integer eigenvalue j_z. Combining the latter with f, we obtain the parameter $\tilde{j}_z = j_z + f$. In addition, we perform the transformation

$$h_{2D} = \sqrt{\rho}\, h_{3D}\, \frac{1}{\sqrt{\rho}} \tag{A9}$$

in order to have the Euclidean scalar product in the effective two-dimensional model formulated in the half-plane $(x > 0, z)$. Finally, renaming $\rho \to x$, we obtain the Hamiltonian (2).

2. Coordinate transformation

The Hamiltonian (1) for the torus model can be alternatively represented in the new—toroidal-poloidal—coordinate system,

$$x = l_0 + r\sin\theta, \tag{A10}$$

$$z = r\cos\theta, \tag{A11}$$

where $r < r_0 < l_0$ and $\theta \in (-\pi, \pi]$. Transforming the differential operators, we obtain

$$\frac{\partial}{\partial x} = \sin\theta\frac{\partial}{\partial r} + \frac{\cos\theta}{r}\frac{\partial}{\partial\theta} = \frac{1}{2}(\Lambda_+ - \Lambda_-), \tag{A12}$$

$$\frac{\partial}{\partial z} = \cos\theta\frac{\partial}{\partial r} - \frac{\sin\theta}{r}\frac{\partial}{\partial\theta} = \frac{i}{2}(\Lambda_+ + \Lambda_-), \tag{A13}$$

where

$$\Lambda_\pm = -ie^{\pm i\theta}\frac{\partial}{\partial r} \pm \frac{e^{\pm i\theta}}{r}\frac{\partial}{\partial\theta}. \tag{A14}$$

In addition, the two-dimensional Laplace operator reads

$$\nabla_{2D}^2 = \frac{\partial^2}{\partial x^2} + \frac{\partial^2}{\partial z^2} = \frac{\partial^2}{\partial r^2} + \frac{1}{r}\frac{\partial}{\partial r} + \frac{1}{r^2}\frac{\partial^2}{\partial\theta^2}. \tag{A15}$$

Then, we rewrite (2) as

$$h_{2D} = \frac{\sigma_z}{2m^*}\Big[-\nabla_{2D}^2 + \Big(\frac{\tilde{j}_z}{x} + \frac{Bx}{2}\Big)^2 - s_z\Big(\frac{\tilde{j}_z}{x^2} + \frac{B}{2}\Big) - 2m^*\delta\Big] + \alpha\sigma_x\Big[\frac{s_z - is_x}{2}\Lambda_+ + \frac{s_z + is_x}{2}\Lambda_- + s_y\Big(\frac{\tilde{j}_z}{x} + \frac{Bx}{2}\Big)\Big] + \varepsilon_Z s_z. \tag{A16}$$

3. Matrix elements of the 2D model on the basis of Bessel functions

To compute matrix elements in the torus model, we introduce the eigenbasis of $-\nabla_{2D}^2$ with the open boundary

conditions on the disk $r < r_0$,

$$u_{n,j_n}(r,\theta) = \langle r,\theta|n,j_n\rangle = \frac{1}{\sqrt{N_{n,j_n}}} J_n\left(\xi_{n,j_n}\frac{r}{r_0}\right)\frac{e^{in\theta}}{\sqrt{2\pi}}. \tag{A17}$$

It is expressed in terms of the Bessel function J_n and its zeros ξ_{n,j_n} enumerated by $j_n \in \mathbb{N}$ for each $n \in \mathbb{Z}$. Being normalized by

$$N_{n,j_n} = \frac{r_0^2}{2}[J_n'(\xi_{n,j_n})]^2, \tag{A18}$$

the eigenfunctions (A17) obey the orthogonality condition

$$\begin{aligned}\langle n', j'_{n'}|n, j_n\rangle &= \int_0^{2\pi} d\theta \int_0^{r_0} dr\, r\, u^*_{n',j'_{n'}}(r,\theta)\, u_{n,j_n}(r,\theta)\\ &= \delta_{n'n}\delta_{j'_n,j_n}.\end{aligned} \tag{A19}$$

Focusing on the representation (A16), we analytically evaluate the matrix elements

$$\langle n', j'_{n'}| - \nabla^2_{\rm 2D}|n, j_n\rangle = \delta_{n'n}\delta_{j'_n,j_n}\left(\frac{\xi_{n,j_n}}{r_0}\right)^2, \tag{A20}$$

$$\begin{aligned}\langle n', j'_{n'}|\Lambda_\pm|n, j_n\rangle = &-\frac{\delta_{n',n\pm1}}{r_0}(-1)^{j_n+j'_{n\pm1}}\,\mathrm{sgn}\,(n\pm 0^+)\\ &\times\frac{2i\,\xi_{n,j_n}\,\xi_{n\pm1,j'_{n\pm1}}}{\xi^2_{n,j_n}-\xi^2_{n\pm1,j'_{n\pm1}}},\end{aligned} \tag{A21}$$

and numerically we evaluate the matrix elements $\langle n', j'_{n'}|x|n, j_n\rangle$, $\langle n', j'_{n'}|x^2|n, j_n\rangle$, $\langle n', j'_{n'}|\frac{1}{x}|n, j_n\rangle$, $\langle n', j'_{n'}|\frac{1}{x^2}|n, j_n\rangle$.

Choosing an appropriate high-energy cutoff, we diagonalize the matrix Hamiltonian and compare its spectrum in Fig. 5 with the tb model spectrum presented in Fig. 2(a).

4. Effective surface model

To derive an effective surface model, we apply the following unitary transformation to the Hamiltonian (A16):

$$U_\theta = e^{-\frac{i}{2}\theta}e^{\frac{i}{2}s_y\theta}, \tag{A22}$$

which maintains the periodic boundary conditions in the θ variable.

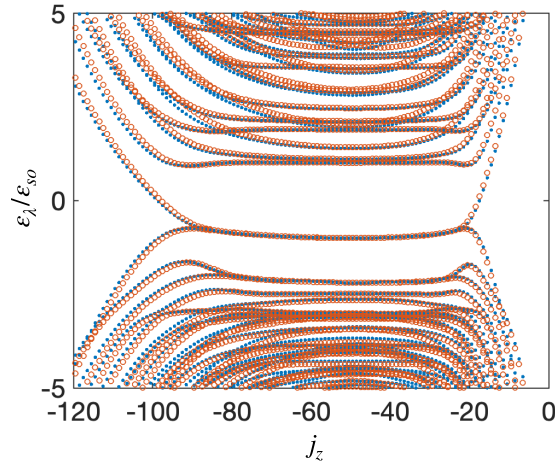

FIG. 5. Comparison of the low-energy states calculated within the tb model (blue dots) and the continuum model (orange circles) at $f = 0$ (same parameters as in Figs. 2 and 3). Small deviations can be consistently eliminated by reducing the lattice constant value in the tb model and by increasing the high-energy cutoff in the continuum model.

The transformation (A22) acts as follows:

$$U_\theta s_x U_\theta^\dagger = s_x\cos\theta + s_z\sin\theta, \tag{A23}$$

$$U_\theta s_z U_\theta^\dagger = -s_x\sin\theta + s_z\cos\theta, \tag{A24}$$

$$U_\theta(s_x\sin\theta + s_z\cos\theta)U_\theta^\dagger = s_z, \tag{A25}$$

$$U_\theta(s_x\cos\theta - s_z\sin\theta)U_\theta^\dagger = s_x, \tag{A26}$$

and

$$U_\theta\frac{\partial}{\partial\theta}U_\theta^\dagger = \frac{\partial}{\partial\theta} + i\frac{1-s_y}{2}. \tag{A27}$$

The listed transformed operators are to replace in (A16) their initial counterparts.

In addition to (A22), we transform wave functions $\Psi \to \sqrt{r}\Psi$ in order to absorb the functional determinant r into the wave function's definition. Accordingly, we transform all operators, $O \to \sqrt{r}O\frac{1}{\sqrt{r}}$. Thus we get

$$\begin{aligned}\tilde h_{\rm 2D} &= \sqrt{r}U_\theta h_{\rm 2D}U_\theta^\dagger\frac{1}{\sqrt{r}}\\ &= \frac{\sigma_z}{2m^*}\left[-\frac{\partial^2}{\partial r^2} + \frac{1}{r^2}\left(-i\frac{\partial}{\partial\theta}+\frac{1}{2}\right)^2 - \frac{s_y}{r^2}\left(-i\frac{\partial}{\partial\theta}+\frac{1}{2}\right) + \left(\frac{\tilde j_z}{x}+\frac{Bx}{2}\right)^2 - (-s_x\sin\theta + s_z\cos\theta)\left(\frac{\tilde j_z}{x^2}+\frac{B}{2}\right) - 2m^*\delta\right]\\ &\quad + \alpha\sigma_x\left[-is_z\frac{\partial}{\partial r} + \frac{s_x}{r}\left(-i\frac{\partial}{\partial\theta}+\frac{1}{2}\right) + s_y\left(\frac{\tilde j_z}{x}+\frac{Bx}{2}\right)\right] + \varepsilon_Z(-s_x\sin\theta + s_z\cos\theta).\end{aligned} \tag{A28}$$

For a sufficiently large radius $r_0 \gg l_{\rm so}$, we can neglect the curvature effects in deriving the low-energy theory for surface states. Considering first the radial part of (A28),

$$\tilde h^{(0)}_{\rm 2D} = \frac{\sigma_z}{2m^*}\left[-\frac{\partial^2}{\partial r^2} - 2m^*\delta\right] - i\alpha\sigma_x s_z\frac{\partial}{\partial r}, \tag{A29}$$

we establish that surface states are zero-energy states of this Hamiltonian, and their radial dependence is captured by the ansatz

$$\psi_{\rm surface}(r) \propto e^{-(r_0-r)/l_{\rm so}}\sin[k_F(r_0-r)], \tag{A30}$$

with $k_F = \sqrt{2m^*\delta - (m^*\alpha)^2}$. Inserting it into (A29), we obtain an equation for the spinor structure $|\chi_{\text{surface}}\rangle$ of the surface states,

$$\frac{1-\sigma_y s_z}{2}|\chi_{\text{surface}}\rangle = 0. \tag{A31}$$

Hence we find the projector onto the surface states subspace,

$$P_{\text{surface}} = \frac{1+\sigma_y s_z}{2}. \tag{A32}$$

Projecting (A28) onto the surface states subspace, averaging the radial degree of freedom in the state (A30), and additionally approximating $\langle g(r)\rangle \approx g(r_0)$, we obtain the effective low-energy theory for the surface states,

$$h_{\text{surface}} = P_{\text{surface}}\left[\sigma_z s_y\left(\frac{\alpha}{r_0} - \frac{1}{2m^* r_0^2}\right)\left(-i\frac{\partial}{\partial\theta} + \frac{1}{2}\right) - \sigma_z s_x\left(\frac{\alpha}{x} - \frac{\sin\theta}{2m^* x^2}\right)\left(\tilde{j}_z + \frac{Bx^2}{2}\right) + \varepsilon_Z s_z\cos\theta\right]P_{\text{surface}}, \tag{A33}$$

with $x = l_0 + r_0\sin\theta$.

5. Hinge and Landau surface states in the torus model

a. Right and left hinge states

To describe the right and left hinge states, we consider $l_0 \gg r_0 \gg l_{\text{so}}$ in the effective surface Hamiltonian (A33) and derive

$$h_{\text{surface}} \approx P_{\text{surface}}\left[\sigma_z s_y\frac{\alpha}{r_0}\left(-i\frac{\partial}{\partial\theta} + \frac{1}{2}\right) - \sigma_z s_x\frac{\alpha}{l_0}\left(\tilde{j}_z + \frac{Bx^2}{2}\right) + \varepsilon_Z s_z\cos\theta\right]P_{\text{surface}}. \tag{A34}$$

Near $\theta = \pm\frac{\pi}{2}$, we approximate

$$h_{\text{surface}} \approx P_{\text{surface}}\left[-i\sigma_z s_y\frac{\alpha}{r_0}\frac{\partial}{\partial\theta} + \sigma_z s_y\frac{\alpha}{2r_0} - \sigma_z s_x\frac{\alpha}{l_0}\left(\tilde{j}_z + \frac{B(l_0 \pm r_0)^2}{2}\right) + \varepsilon_Z s_z\cos\theta\right]P_{\text{surface}}. \tag{A35}$$

At $\tilde{j}_z \approx -\frac{B(l_0\pm r_0)^2}{2}$, we solve the eigenvalue problem for a hinge state with nearly zero energy,

$$\left[-i\sigma_z s_y\frac{\alpha}{r_0}\frac{\partial}{\partial\theta} + \varepsilon_Z s_z\cos\theta\right]e^{\pm\varepsilon_Z\frac{r_0}{\alpha}\sin\theta}|\tilde{\chi}_{R,L}\rangle = 2\varepsilon_Z e^{\pm\varepsilon_Z\frac{r_0}{\alpha}\sin\theta}s_z\cos\theta\frac{1\mp\sigma_z s_x}{2}|\tilde{\chi}_{R,L}\rangle = 0. \tag{A36}$$

Thus $|\tilde{\chi}_{R,L}\rangle$ is a simultaneous eigenstate (to the eigenvalue $+1$) of the projectors $P_{\text{surface}} = \frac{1+\sigma_y s_z}{2}$ and $\frac{1\pm\sigma_z s_x}{2}$. It reads

$$|\tilde{\chi}_{R,L}\rangle = \frac{1}{2}\left[\begin{pmatrix}1\\ i\end{pmatrix}_{\sigma_z}\begin{pmatrix}1\\ 0\end{pmatrix}_{s_z} \pm \begin{pmatrix}1\\ -i\end{pmatrix}_{\sigma_z}\begin{pmatrix}0\\ 1\end{pmatrix}_{s_z}\right]. \tag{A37}$$

Noticing that $\langle\tilde{\chi}_{R,L}|\sigma_z s_y|\tilde{\chi}_{R,L}\rangle = 0$, we perturbatively evaluate the energy dispersion in $\tilde{j}_z$,

$$\varepsilon_{R,L}(\tilde{j}_z) \approx -\langle\tilde{\chi}_{R,L}|\sigma_z s_x|\tilde{\chi}_{R,L}\rangle\frac{\alpha}{l_0}\left(\tilde{j}_z + \frac{B(l_0\pm r_0)^2}{2}\right) = \mp\frac{\alpha}{l_0}\left(\tilde{j}_z + \frac{B(l_0\pm r_0)^2}{2}\right). \tag{A38}$$

Undoing the θ-transformation, we obtain

$$|\chi_{R,L}\rangle = U_\theta^\dagger|\tilde{\chi}_{R,L}\rangle = \frac{e^{i\frac{\theta}{2}}}{2}\left[\begin{pmatrix}1\\ i\end{pmatrix}_{\sigma_z}\begin{pmatrix}\cos\frac{\theta}{2}\\ \sin\frac{\theta}{2}\end{pmatrix}_{s_z} \pm \begin{pmatrix}1\\ -i\end{pmatrix}_{\sigma_z}\begin{pmatrix}-\sin\frac{\theta}{2}\\ \cos\frac{\theta}{2}\end{pmatrix}_{s_z}\right]. \tag{A39}$$

Note that $\sigma_x s_y|\chi_{R,L}\rangle = \mp|\chi_{R,L}\rangle$.

b. Top and bottom Landau surface states

To describe the top and bottom Landau surface states, we consider the values $\tilde{j}_z \approx -\frac{Bl_0^2}{2}$, which correspond to the spatial localization at $\sin\theta \approx 0$, that is, $\theta \approx 0$ or $\theta \approx \pi$.

Carefully approximating

$$h_{\text{surface}} \approx P_{\text{surface}}\left[\sigma_x s_x\frac{\alpha}{r_0}\left(-i\frac{\partial}{\partial\theta} + \frac{1}{2}\right) + \sigma_x s_y\frac{\alpha}{l_0}\left(\tilde{j}_z + \frac{Bl_0^2}{2}\right) + \sigma_x s_y\alpha B r_0\sin\theta + \varepsilon_Z s_z\cos\theta\right], \tag{A40}$$

we extract the leading-order Hamiltonian

$$h_{\text{TB}}^{(0)} \approx -i\sigma_x s_x P_{\text{surface}}\frac{\alpha}{r_0}\left[\frac{\partial}{\partial\theta} - s_z B r_0^2\sin\theta\right]. \tag{A41}$$

It possesses the two zero-energy solutions: the top and bottom states $\propto e^{\pm Br_0^2\cos\theta}$ with $s_z = \mp 1$, which are localized near $\theta \approx 0$ and $\theta \approx \pi$, respectively. Their spinor structure is determined by the relations $\sigma_y s_z = +1$ and

$s_z = \mp 1$:

$$|\tilde{\chi}_T\rangle = \frac{1}{\sqrt{2}}\begin{pmatrix}1\\-i\end{pmatrix}_{\sigma_z}\begin{pmatrix}0\\1\end{pmatrix}_{s_z}, \tag{A42}$$

$$|\tilde{\chi}_B\rangle = \frac{1}{\sqrt{2}}\begin{pmatrix}1\\i\end{pmatrix}_{\sigma_z}\begin{pmatrix}1\\0\end{pmatrix}_{s_z}. \tag{A43}$$

Undoing the θ-transformation, we obtain

$$|\chi_T\rangle = U_\theta^\dagger|\tilde{\chi}_T\rangle = \frac{e^{\frac{i}{2}\theta}}{\sqrt{2}}\begin{pmatrix}1\\-i\end{pmatrix}_{\sigma_z}\begin{pmatrix}-\sin\frac{\theta}{2}\\ \cos\frac{\theta}{2}\end{pmatrix}_{s_z}, \tag{A44}$$

$$|\chi_B\rangle = U_\theta^\dagger|\tilde{\chi}_B\rangle = \frac{e^{\frac{i}{2}\theta}}{\sqrt{2}}\begin{pmatrix}1\\i\end{pmatrix}_{\sigma_z}\begin{pmatrix}\cos\frac{\theta}{2}\\ \sin\frac{\theta}{2}\end{pmatrix}_{s_z}. \tag{A45}$$

The energy of these states is obtained from the perturbative $\tilde{j}_z$-independent correction

$$\varepsilon_{T,B} \approx -\varepsilon_Z. \tag{A46}$$

The degeneracy is lifted by the exponentially small overlap of the two states, which leads to the symmetric and antisymmetric combinations of the top and bottom states. In particular, projecting the initially neglected small terms

$$\Delta h_{\text{surface}} \approx P_{\text{surface}} \times\left[\sigma_x s_x\frac{\alpha}{2r_0} + \sigma_x s_y\frac{\alpha}{l_0}\left(\tilde{j}_z + \frac{Bl_0^2}{2}\right) + \varepsilon_Z s_z\cos\theta\right] \tag{A47}$$

onto the subspace spanned by the top and bottom states found above in the leading approximation, we obtain the following effective 2×2 Hamiltonian:

$$\Delta h^{\text{eff}}_{\text{surface}} = -\varepsilon_Z + \frac{\alpha}{2r_0\mathcal{N}} \times\begin{pmatrix}0 & i+\frac{2r_0}{l_0}\left(\tilde{j}_z+\frac{Bl_0^2}{2}\right)\\ -i+\frac{2r_0}{l_0}\left(\tilde{j}_z+\frac{Bl_0^2}{2}\right) & 0\end{pmatrix}, \tag{A48}$$

where

$$\mathcal{N} = \frac{1}{2\pi}\int_{-\pi}^{\pi} d\theta e^{\pm 2Br_0^2\cos\theta} \approx \frac{e^{2Br_0^2}}{2\sqrt{\pi Br_0^2}}, \quad Br_0^2 \gg 1. \tag{A49}$$

Diagonalizing (A48), we obtain the energy splitting

$$\Delta\varepsilon(\tilde{j}_z) \approx \frac{\alpha}{r_0\mathcal{N}}\sqrt{1+\frac{4r_0^2}{l_0^2}\left(\tilde{j}_z+\frac{Bl_0^2}{2}\right)^2}. \tag{A50}$$

It is minimal in the plateau's middle,

$$\Delta\varepsilon\left(\tilde{j}_z \approx -\frac{Bl_0^2}{2}\right) \approx \frac{\alpha}{r_0\mathcal{N}} \approx 2\alpha\sqrt{\pi B}e^{-Br_0^2}, \tag{A51}$$

giving an estimate of the splitting between ε_{-1} and ε_0 bands.

APPENDIX B: VANISHING CONTRIBUTION TO THE BOUNDARY CHARGE FROM THE BANDS $\varepsilon_{\lambda\leqslant -1}$

Studying numerically the quantity

$$\tilde{Q}_B^{R,L}(\tilde{j}_z) = \sum_{\lambda\leqslant -1}\left[\bar{Q}_{B,\lambda}^{R,L}(\tilde{j}_z) - \bar{Q}_{B,\lambda}^{R,L}(|\tilde{j}_z|\to\infty)\right], \tag{B1}$$

we obtain the results shown in Fig. 6(a). Evaluating the sum $\sum_{j_z}\tilde{Q}_B^{R,L}(j_z+f)$, we obtain a small number of $O(1)$ which is constant for all values of f [see Fig. 6(b)]. Then

$$\sum_{\lambda\leqslant -1}\sum_{j_z}\left[\bar{Q}_{B,\lambda}^{R,L}(j_z+f) - \bar{Q}_{B,\lambda}^{R,L}(j_z)\right] = \sum_{j_z}\left[\tilde{Q}_B^{R,L}(j_z+f) - \tilde{Q}_B^{R,L}(j_z)\right] = 0, \tag{B2}$$

which proves the vanishing contribution of the bands $\varepsilon_{\lambda\leqslant -1}$ to the boundary charge.

APPENDIX C: DETAILS OF THE TIGHT-BINDING MODELING AND CALCULATION OF THE BOUNDARY CHARGE

1. 2D tight-binding model as a discrete version of the continuum model

To numerically solve the effective 2D continuum model shown in Eq. (2), we first replace the continuous coordinates by discrete sites, and we substitute the derivatives with finite differences [67]. The site labeled by i has the position $\mathbf{r}_i = ma\hat{\mathbf{e}}_x + na\hat{\mathbf{e}}_z$, where m, n are integer numbers, a is a lattice constant chosen to be small as compared to other scales in the model, and $\hat{\mathbf{e}}_\zeta$ with $\zeta = x, z$ is the unit vector pointing towards the ζ-direction. In the lattice representation, the differential operators are replaced as $\frac{\partial^2}{\partial\zeta^2}\psi(x,z)|_{\mathbf{r}_i} = \frac{1}{a^2}[\psi(\mathbf{r}_i + a\hat{\mathbf{e}}_\zeta) - 2\psi(\mathbf{r}_i) + \psi(\mathbf{r}_i - a\hat{\mathbf{e}}_\zeta)]$ and $\frac{\partial}{\partial\zeta}\psi(x,z)|_{\mathbf{r}_i} = \frac{1}{a}[\psi(\mathbf{r}_i + a\hat{\mathbf{e}}_\zeta) - \psi(\mathbf{r}_i)]$, where $\psi(x,z)$ is the 2D wave function. With this approximation, we get the matrix representation of the Hamiltonian (2), which is in the tb form and only contains the nearest coupling terms between adjacent sites. To get the geometry of a disk as shown in Fig. 1(b), we consider a rectangular grid with length and width slightly larger than $2r_0$, and we choose the center of the grid to coincide with that of the disk. By applying an infinitely large on-site potential outside the disk boundary, we achieve a realization of the open boundary conditions on the disk boundary. By exact diagonalization of the Hamiltonian matrix, we obtained the band structure, the density of states, and the boundary charge. In Fig. 5 we compare the low-energy states obtained from the 2D tb model by setting $a = l_{\text{so}}/5$, and the one from directly solving the continuum model (2) in the basis introduced in Appendix A 3. The good agreement validates the accuracy of the 2D tb approximation.

2. Tight-binding Hamiltonian of the 3D TI under magnetic fields

To calculate the boundary charge in the presence of disorder potential, we use a 3D tb Hamiltonian of a TI [68,69]. The Hamiltonian defined on a cubic lattice is written as

$$H_{\text{3D}}^{\text{tb}} = \sum_i t|\mathbf{r}_i\rangle\mathcal{M}_i\langle\mathbf{r}_i| + \sum_i\sum_{\zeta=x,y,z} t\left(|\mathbf{r}_i + a_{\text{3D}}\hat{\mathbf{e}}_\zeta\rangle\mathcal{T}_\zeta e^{i\phi_{\mathbf{r}_i,\mathbf{r}_i+a_{\text{3D}}\hat{\mathbf{e}}_\zeta}}\langle\mathbf{r}_i| + \text{H.c.}\right), \tag{C1}$$

where $|\mathbf{r}_i\rangle$ is the Wannier basis denoting the lattice site with real-space position $\mathbf{r}_i$, and it has both orbital and

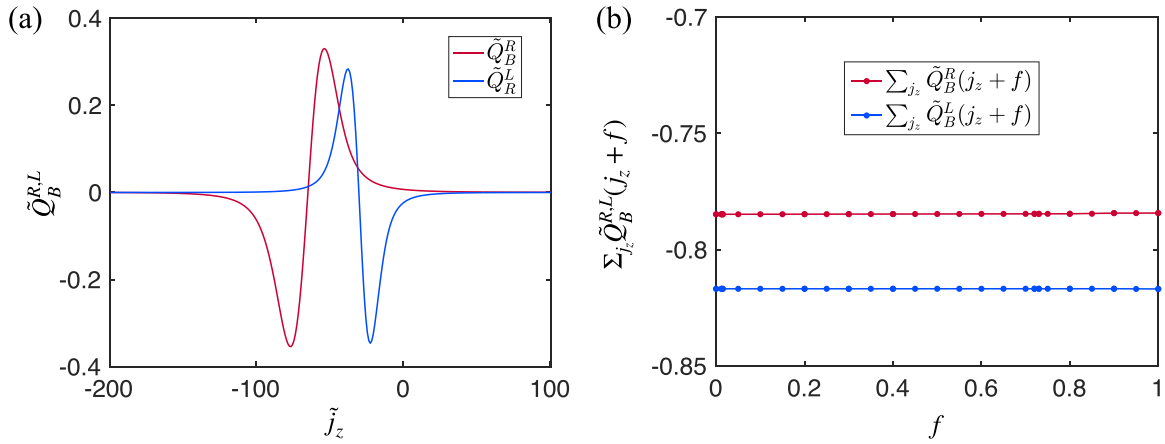

FIG. 6. (a) $\tilde{j}_z$-resolved boundary charges as defined in Eq. (B1). (b) The summed values $\sum_{j_z} \tilde{Q}_B^{R,L}(j_z+f)$ (same parameters as in Figs. 2 and 3). In the numerical summation, j_z ranges from -199.5 to 100.5.

spin degrees of freedom encoded in the components $|\mathbf{r}_i\rangle = (|\mathbf{r}_i^{1\uparrow}\rangle, |\mathbf{r}_i^{1\downarrow}\rangle, |\mathbf{r}_i^{2\uparrow}\rangle, |\mathbf{r}_i^{2\downarrow}\rangle)^T$ with $\sigma = 1, 2$ and $s = \uparrow, \downarrow$. Here t and a_{3D} represent the hopping amplitude and the lattice constant of the 3D tb model, respectively. The on-site matrix elements are given by $\mathcal{M}_i = m_0\sigma_z + \Delta_z s_z + U_i \equiv \mathcal{M}_0 + U_i$, where Δ_z is the dimensionless Zeeman energy in units of t, and U_i is the on-site disorder potential, which is uniformly distributed within $[-W/2, W/2]$, with W being the characteristic disorder strength. The hopping matrix elements are given by $\mathcal{T}_\zeta = -\frac{\alpha_{tb}}{2i}\sigma_x s_\zeta - \frac{m_1}{2}\sigma_z$.

The orbital effect of the magnetic field is included by adding a phase factor $\phi_{\mathbf{r}_i,\mathbf{r}_i+a_{3D}\hat{\mathbf{e}}_\zeta} = -2\pi \int_{\mathbf{r}_i}^{\mathbf{r}_i+a_{3D}\hat{\mathbf{e}}_\zeta} \mathbf{A}\cdot d\mathbf{r}/\phi_0$ to the hopping matrices $\mathcal{T}_\zeta$, with the vector potential $\mathbf{A}$ containing contributions that generate both the uniform magnetic field $\mathbf{B}$ and the AB flux. In the real calculations to get the geometry of a torus, we start with a cuboid of the size $N_x \times N_y \times N_z \times a_{3D}^3$, and we restrict the actual volume to the interior of the torus $(\sqrt{x^2+y^2}-l_0)^2 + z^2 < r_0^2$ by applying an infinite on-site potential outside it. To simplify the numerical calculation, we use the Landau gauge $(-By, 0, 0)$ for $\mathbf{A}_B$, and the discontinuous gauge $2\pi f\delta(\varphi)\nabla\varphi$ for $\mathbf{A}_\phi$.

Let us now relate the parameters of the above-introduced 3D tb model to the parameters of the Hamiltonian (1) in the main text. To this end, we first omit in the 3D tb Hamiltonian the disorder term U_i and the orbital effects of the magnetic fields, and we relax the boundary conditions. This restores the translational invariance and allows us to introduce the Bloch Hamiltonian

$$H_{3D}^{tb} = \sum_{\mathbf{k}} |\mathbf{k}\rangle \left[t\mathcal{M}_0 + \sum_{\zeta=x,y,z} \left(t\mathcal{T}_\zeta e^{-i\mathbf{k}\cdot\hat{\mathbf{e}}_\zeta a_{3D}} + t\mathcal{T}_\zeta^\dagger e^{i\mathbf{k}\cdot\hat{\mathbf{e}}_\zeta a_{3D}} \right) \right]$$
$$\langle\mathbf{k}| \equiv \sum_{\mathbf{k}} |\mathbf{k}\rangle h_{3D}(\mathbf{k}) \langle\mathbf{k}|, \tag{C2}$$

with

$$\begin{aligned} h_{3D}(\mathbf{k}) = {} & t\Delta_z s_z + t\alpha_{tb}\sigma_x (s_x \sin k_x a_{3D} \\ & + s_y \sin k_y a_{3D} + s_z \sin k_z a_{3D}) \\ & + t\sigma_z [m_0 - m_1(\cos k_x a_{3D} + \cos k_y a_{3D} + \cos k_z a_{3D})]. \end{aligned} \tag{C3}$$

Approximating this expression around the $\mathbf{\Gamma} = (0,0,0)$ point in the Brillouin zone by virtue of the relations $\sin k_\zeta a_{3D} \approx k_\zeta a_{3D}$ and $\cos k_\zeta a_{3D} \approx 1 - \frac{1}{2}k_\zeta^2 a_{3D}^2$, we get

$$\begin{aligned} h_{3D}(\mathbf{k}) \approx {} & t\sigma_z s_0 \left[\frac{m_1 a_{3D}^2}{2} k^2 - (3m_1 - m_0) \right] \\ & + t\alpha_{tb} a_{3D} \sigma_x (\mathbf{k}\cdot\mathbf{s}) + t\Delta_z s_z. \end{aligned} \tag{C4}$$

To achieve the equivalence between (C4) and (1), we identify $\frac{tm_1 a_{3D}^2}{2} = \frac{1}{2m^*}$, $t(3m_1 - m_0) = \delta$, $t\alpha_{tb}a_{3D} = \alpha$, and $t\Delta_z = \varepsilon_Z$. By setting the hopping energy $t = \varepsilon_{so}$ and the lattice constant $a_{3D} = l_{so}$, we get the following values of the dimensionless parameters in the 3D tb Hamiltonian: $m_1 = 2$, $m_0 = 3$, $\alpha_{tb} = 2$, and $\Delta_z = 1$, in accordance with the parameter values of the Hamiltonian (1) specified in the caption of Fig. 2. The orbital effect of the magnetic field is incorporated by substituting $\mathbf{k}$ with $\mathbf{k} + \mathbf{A}$. The magnetic flux through each unit cell projected onto the x-y plane generated by the uniform magnetic field $\mathbf{B}$ is calculated to be $\phi_{xy} = Ba_{3D}^2 = 1$. This observation helps us to calculate numerically the phase factor $\phi_{\mathbf{r}_i,\mathbf{r}_i+a_{3D}\hat{\mathbf{e}}_\zeta}$ appearing in (C1).

Having established the correspondence in the low-energy description between the 3D tb Hamiltonian and its continuum model counterpart, we further use the tb model to evaluate the boundary charge in the presence of on-site disorder breaking the rotational symmetry.

3. Green's function method in calculating the boundary charge

Since we have used a 3D cuboid to simulate the torus model, the starting lattice has $N_x \times N_y \times N_z$ sites. Accounting for the spin and orbital degrees of freedom, we obtain the Hilbert space dimension of the tb Hamiltonian to be $N_H = 4 \times N_x \times N_y \times N_z$. For the torus with $l_0 = 10\, l_{so}$ and $r_0 = 5\, l_{so}$, we need at least $N_x = N_y = 31$ and $N_z = 11$. Exactly diagonalizing such a huge matrix of the dimension $N_H = 42\,284$ requires a large amount of virtual computer memory rendering the calculation very time-consuming. Instead of this direct approach, we adhere to the recursive Green's-function method [70] to calculate the boundary charge. This method allows us to separate the task into hundreds of jobs which

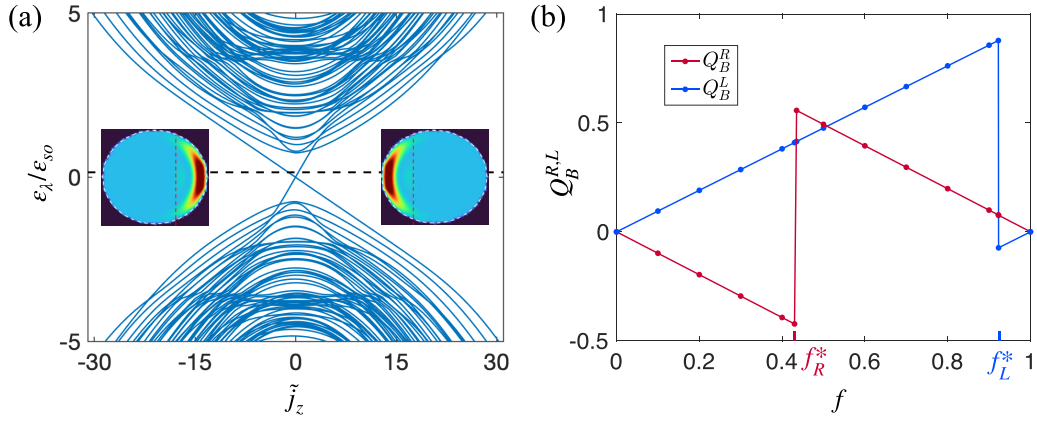

FIG. 7. (a) Low-energy spectrum of the torus model (in units of spin-orbit energy $\varepsilon_{\rm so}$) without the magnetic orbital effect ($B = 0$). The parameters we use here are $\delta = 3\,\varepsilon_{\rm so}$, $l_0 = 10\,l_{\rm so}$, $r_0 = 5\,l_{\rm so}$, and $\varepsilon_Z = \varepsilon_{\rm so}$. The chemical potential is set to $\mu = 0.15$. (b) Right and left boundary charges as functions of f feature the linear slopes with the values -0.9859 and 0.9523, respectively, which are complemented by the jumps with the corresponding amplitudes at the flux values $f_R^* \approx 0.43$ and $f_L^* \approx 0.92$. The actual numerical summation runs over the j_z range from -149.5 to 150.5, which is sufficient to ensure convergence. The width of the boundary regions is $d = 3\,l_{\rm so}$. It accommodates approximately 98.53% (95.23%) of the weight of the right (left) hinge state at the energy $\approx 0.1508\,\varepsilon_{\rm so}$ ($\approx 0.1490\,\varepsilon_{\rm so}$) [see the insets in (a)], and this explains the deviation of the jump (and the slope) size from the universal unit value.

can be computed in parallel on a high-performance computing cluster.

The total charge within the region $\mathcal{B}$ below the chemical potential of the 3D lattice system is defined as $Q^{\rm tb}_{\mathcal{B}} = \int_{-\infty}^{\infty} d\varepsilon \sum_{i\in\mathcal{B}} \Theta(\mu-\varepsilon)\rho_i(\varepsilon) = \sum_{i\in\mathcal{B}} Q^{\rm tb}(i)$, where $Q^{\rm tb}(i) \equiv \int_{-\infty}^{\mu} d\varepsilon \rho_i(\varepsilon) = \sum_{\varepsilon_\lambda \leqslant \mu} \rho_i(\varepsilon_\lambda)$ is the total charge at site i. Here ε_λ is the discrete eigenvalues of the isolated system with eigenstate $|\lambda\rangle$, $\rho_i(\varepsilon_\lambda) = |\langle \mathbf{r}_i|\lambda\rangle|^2$, and $\rho_i(\varepsilon) = \sum_{\varepsilon_\lambda} \rho_i(\varepsilon_\lambda)\delta(\varepsilon-\varepsilon_\lambda)$ is the local density of states at site i. Further, we represent

$$Q^{\rm tb}(i) = \frac{1}{2\pi i}\int_{\mathcal{C}} dz\, G_i(z) \tag{C5}$$

in terms of the site-diagonal components $G_i(z) = \langle \mathbf{r}_i|G(z)|\mathbf{r}_i\rangle = \sum_{\varepsilon_\lambda} \frac{\rho_i(\varepsilon_\lambda)}{z-\varepsilon_\lambda}$ of the Green's function $G(z) = (z - H^{\rm tb}_{\rm 3D})^{-1}$. In this expression, a counterclockwise integration path $\mathcal{C}$ in the complex-z plane encompasses the poles of $G_i(z)$ at $z = \varepsilon_\lambda$ lying below the chemical potential μ.

To facilitate the integration, we use a rectangular loop $\mathcal{C}$ with the four corners in the complex plane: $z_{1(2)} = \mu + 0^+ \mp b_M i$ and $z_{3(4)} = -a_M \pm b_M i$, where b_M and a_M are both large and positive real numbers denoting the absolute maximum values of the imaginary and real part of z, respectively. This allows us to express

$$\begin{aligned} Q^{\rm tb}(i) = {} & \frac{1}{2\pi}\int_{-b_M}^{b_M} db\,{\rm Re}[G_i(\mu+0^+ + bi)] \\ & + \frac{1}{\pi}\int_{-a_M}^{\mu+0^+} da\,{\rm Im}[G_i(a-b_M i)] \\ & - \frac{1}{2\pi}\int_{-b_M}^{b_M} db\,{\rm Re}[G_i(-a_M+bi)]. \end{aligned} \tag{C6}$$

The last two integrals are insensitive to the parameter f (which can always be numerically tested), because they account for contributions from the states $|\varepsilon_\lambda| \sim a_M, b_M$ lying far below the Fermi surface. This observation leads us to the operational formula

$$Q^{\rm tb}(i) = \frac{1}{2\pi}\int_{-b_M}^{b_M} db\,{\rm Re}[G_i(\mu+0^+ + bi)] + {\rm const.} \tag{C7}$$

To calculate $G_i(z)$, we employ the recursive Green's-function method [70], which avoids a direct calculation of the inverse of the huge Hamiltonian matrix.

APPENDIX D: 3D QHE IN THE ABSENCE OF THE ORBITAL *B*-FIELD EFFECT

In Fig. 7(a) we show the band structure of our model in the absence of the orbital B-field effect. It features the two midgap modes of the R and L hinge states traversing the surface gap and connecting the hinge modes with bulk surface states. In Fig. 7(b) we show the right and left boundary charges [defined within the same boundary regions as in Fig. 1(b)], which receive contributions from all occupied states below the chemical potential μ. They feature the linear dependencies on f with the slope values -0.9859 and 0.9523, which are complemented by the jumps of the corresponding sizes.

In the absence of the orbital B-field effect, there is no plateau region of surface states connecting the R and L hinges. Therefore, for the analytical explanation it is easier to consider the total boundary charge and write it as a sum over all total angular momenta

$$Q_B^{R,L}(f) = \sum_{j_z}\left[\bar{Q}_B^{R,L}(j_z+f) - \bar{Q}_B^{R,L}(j_z)\right], \tag{D1}$$

where $\bar{Q}_B^{R,L}(j_z+f)$ includes the sum over all bands and the condition that the energy must be smaller than μ,

$$\bar{Q}_B^{R,L}(\tilde{j}_z) = \sum_{\lambda} \Theta(\mu - \varepsilon_\lambda(\tilde{j}_z))\bar{Q}_{B,\lambda}^{R,L}(\tilde{j}_z). \tag{D2}$$

To estimate the typical scale Δj_z on which $\bar{Q}_B^{R,L}(j_z+f)$ is expected to vary on j_z (up to jumps occurring when the energy

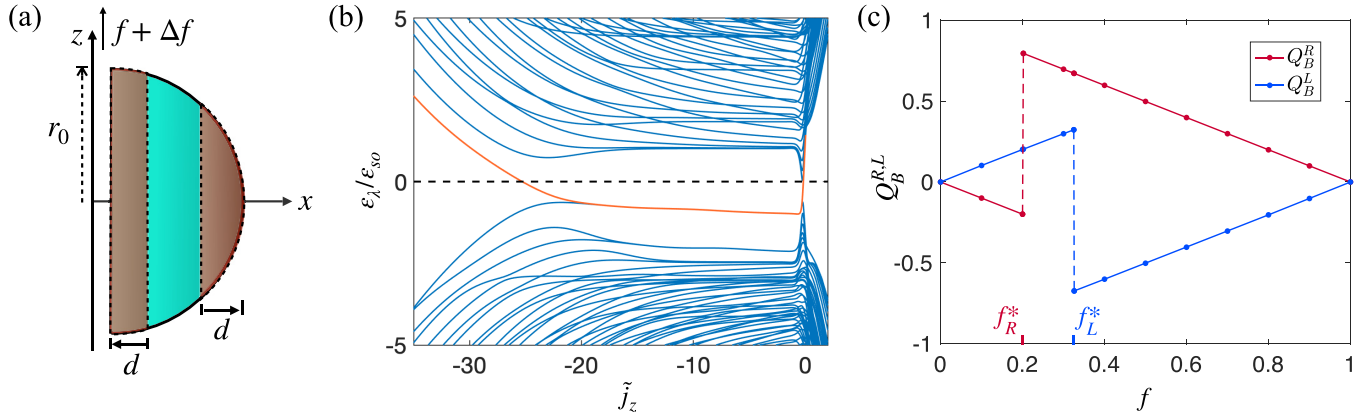

FIG. 8. (a) Sketch of the half-disk. (b) Low-energy spectrum of the half-disk model at $B \neq 0$ in units of spin-orbit energy $\varepsilon_{\rm so}$. The parameters we use here are $\delta = 3\,\varepsilon_{\rm so}$, $l_B = l_{\rm so}$, $l_0 = 0$, $r_0 = 8\,l_{\rm so}$, and $\varepsilon_Z = \varepsilon_{\rm so}$. The lattice constant is chosen to be $a = l_{\rm so}/3$. The chemical potential is set to $\mu = 0$. (c) Right and left boundary charges as functions of f feature the linear slopes with the values -0.9962 and 0.9993, respectively, which are complemented by the unit jumps at the flux values $f_R^* \approx 0.2$ and $f_L^* \approx 0.32$. The width of the boundary regions is $d = 2.5\,l_{\rm so}$. The actual numerical summation runs over the j_z range from -59.5 to 30.5, which is sufficient to ensure convergence.

of the highest valence band crosses the chemical potential), we have to compare the scale of the momentum parallel to the surface $\sim j_z/l_0$ with various other inverse lengthscales appearing in the Hamiltonian (A16) (such as $\varepsilon_Z/\alpha \sim l_{\rm so}/l_Z^2$, $m^*\alpha = 1/l_{\rm so}$, or $\sqrt{m^*\delta}$). Since all these inverse lengthscales are independent of l_0, the scale Δj_z will always increase with the torus radius l_0 and we find, analogous to the arguments presented in the main text, that the boundary charge $Q_B^{R,L}(f)$ is dominated by its linear term to any desired degree of accuracy by increasing the torus radius. The linear behavior together with the jump properties and the periodicity of $Q_B^{R,L}(f)$ then prove the universal slopes of $Q_B^{R,L}(f)$ in the same manner as discussed in the main text.

In the presence of strong orbital fields $l_B \sim l_Z$ we note that the typical scale Δj_z arises from the combination $j_z + f + Bx^2/2$ in the Hamiltonian (A16). With $x = l_0 + r\sin\theta$ and $B = 1/l_B^2$, we get

$$\frac{Bx^2}{2} = \frac{l_0^2}{2l_B^2} + \frac{rl_0}{l_B^2}\sin\theta + \frac{r^2}{2l_B^2}\sin^2\theta. \tag{D3}$$

The first term leads to an unimportant shift of j_z. With $\sin\theta \sim O(1)$ and $r \sim r_0 < l_0$, the last two terms determine the scale $\Delta j_z \sim l_0 r_0/l_B^2$, which is of the order of the number of fluxes threaded through the torus surface from the orbital field; cf. the main text.

As a result, for any value of the orbital field B, we obtain that the scale Δj_z increases linearly with the torus radius l_0. Therefore, the universal form of the boundary charge is unaffected by the orbital effects. We note that our estimate of the higher-order derivatives

$$\frac{d^n}{df^n}Q_B^{R,L}(f) \sim \frac{1}{(\Delta j_z)^{n-1}} \tag{D4}$$

is quite conservative. The reason is that the sum over j_z for the higher-order derivatives $(\frac{d}{d\tilde{j}_z})^n \bar{Q}_B^{R,L}(\tilde{j}_z)$, with $n \geqslant 2$, of (D1) contains many terms with different signs that partially cancel each other. This can be seen from replacing sums by integrals and noting that the asymptotic values of $(\frac{d}{d\tilde{j}_z})^{n-1}\bar{Q}_B^{R,L}(\tilde{j}_z)$, with $n \geqslant 2$, go to zero for $\tilde{j}_z \to \pm\infty$. The same holds close to the point where the highest valence band leads to a jump of $\bar{Q}_B^{R,L}(\tilde{j}_z)$ when some hinge modes cross the chemical potential. The variation in j_z becomes very weak close to the jumping point if the boundary region is chosen much larger than the localization length of all hinge modes. The vanishing integral of all higher-order derivatives with $n \geqslant 2$ then indicates that also the sum is expected to be very small providing another reason why the linear behavior is so robust with an error expected to be even much smaller than $1/\Delta j_z$. This is indeed the case in Fig. 7, where $\Delta j_z \sim l_0/l_{\rm so} = 10$, but the deviation from the linear behavior is much smaller than 10%.

APPENDIX E: 3D QHE IN THE SPHERICAL GEOMETRY

In Fig. 8 we show a two-dimensional projection of the sphere in the right half-plane ($x > 0, z$) appearing in the form of the half-disk. The model (with the magnetic orbital effects) is equipped with the open boundary conditions along its whole circumference including the vertical section. Vanishing of the wave function on the vertical section is equivalent to drilling an infinitesimally thin hole in the sphere, which allows for an insertion of the AB flux.

The band structure shown in Fig. 8(b) features a distinguished band (marked in orange) of states residing along the circumference of the half-disk. The states on the negative gentle slope are the hinge states localized near the spherical equator, while the states on the positive steep slope are spatially localized along the vertical axis.

In Fig. 8(c) the right and left boundary charges in the corresponding brown regions of the panel (a) are shown as functions of f. They receive the whole contribution from the orange band of the panel (b). The calculated slopes are very close to the universal unit values, which is analytically explained by the same arguments as in the torus case.

[1] K. v. Klitzing, G. Dorda, and M. Pepper, New Method for High-Accuracy Determination of the Fine-Structure Constant Based on Quantized Hall Resistance, Phys. Rev. Lett. **45**, 494 (1980).

[2] C. L. Kane and E. J. Mele, Quantum Spin Hall Effect in Graphene, Phys. Rev. Lett. **95**, 226801 (2005).

[3] C. L. Kane and E. J. Mele, Z_2 Topological Order and the Quantum Spin Hall Effect, Phys. Rev. Lett. **95**, 146802 (2005).

[4] B. A. Bernevig, T. L. Hughes, and S.-C. Zhang, Quantum spin hall effect and topological phase transition in hgte quantum wells, Science **314**, 1757 (2006).

[5] M. König, S. Wiedmann, C. Brüne, A. Roth, H. Buhmann, L. W. Molenkamp, X.-L. Qi, and S.-C. Zhang, Quantum spin hall insulator state in hgte quantum wells, Science **318**, 766 (2007).

[6] M. Z. Hasan and C. L. Kane, Colloquium: Topological insulators, Rev. Mod. Phys. **82**, 3045 (2010).

[7] X.-L. Qi and S.-C. Zhang, Topological insulators and superconductors, Rev. Mod. Phys. **83**, 1057 (2011).

[8] F. D. M. Haldane, Model for a Quantum Hall Effect without Landau Levels: Condensed-Matter Realization of the "Parity Anomaly," Phys. Rev. Lett. **61**, 2015 (1988).

[9] C.-X. Liu, X.-L. Qi, X. Dai, Z. Fang, and S.-C. Zhang, Quantum Anomalous Hall Effect in $hg_{1-y}mn_yTe$ Quantum Wells, Phys. Rev. Lett. **101**, 146802 (2008).

[10] A. J. Bestwick, E. J. Fox, X. Kou, L. Pan, K. L. Wang, and D. Goldhaber-Gordon, Precise Quantization of the Anomalous Hall Effect near Zero Magnetic Field, Phys. Rev. Lett. **114**, 187201 (2015).

[11] R. Yu, W. Zhang, H.-J. Zhang, S.-C. Zhang, X. Dai, and Z. Fang, Quantized anomalous hall effect in magnetic topological insulators, Science **329**, 61 (2010).

[12] C.-Z. Chang, J. Zhang, X. Feng, J. Shen, Z. Zhang, M. Guo, K. Li, Y. Ou, P. Wei, L.-L. Wang, Z.-Q. Ji, Y. Feng, S. Ji, X. Chen, J. Jia, X. Dai, Z. Fang, S.-C. Zhang, K. He, Y. Wang, L. Lu, X.-C. Ma, and Q.-K. Xue, Experimental observation of the quantum anomalous hall effect in a magnetic topological insulator, Science **340**, 167 (2013).

[13] J. G. Checkelsky, R. Yoshimi, A. Tsukazaki, K. S. Takahashi, Y. Kozuka, J. Falson, M. Kawasaki, and Y. Tokura, Trajectory of the anomalous hall effect towards the quantized state in a ferromagnetic topological insulator, Nat. Phys. **10**, 731 (2014).

[14] Y. Feng, X. Feng, Y. Ou, J. Wang, C. Liu, L. Zhang, D. Zhao, G. Jiang, S.-C. Zhang, K. He, X. Ma, Q.-K. Xue, and Y. Wang, Observation of the Zero Hall Plateau in a Quantum Anomalous Hall Insulator, Phys. Rev. Lett. **115**, 126801 (2015).

[15] A. Kandala, A. Richardella, S. Kempinger, C.-X. Liu, and N. Samarth, Giant anisotropic magnetoresistance in a quantum anomalous hall insulator, Nat. Commun. **6**, 7434 (2015).

[16] Y. Deng, Y. Yu, M. Z. Shi, Z. Guo, Z. Xu, J. Wang, X. H. Chen, and Y. Zhang, Quantum anomalous hall effect in intrinsic magnetic topological insulator $mnbi_2te_4$, Science **367**, 895 (2020).

[17] C. Liu, Y. Wang, H. Li, Y. Wu, Y. Li, J. Li, K. He, Y. Xu, J. Zhang, and Y. Wang, Robust axion insulator and chern insulator phases in a two-dimensional antiferromagnetic topological insulator, Nat. Mater. **19**, 522 (2020).

[18] J. Ge, Y. Liu, J. Li, H. Li, T. Luo, Y. Wu, Y. Xu, and J. Wang, High-Chern-number and high-temperature quantum Hall effect without Landau levels, Natl. Sci. Rev. **7**, 1280 (2020).

[19] S. X. M. Riberolles, Q. Zhang, E. Gordon, N. P. Butch, L. Ke, J.-Q. Yan, and R. J. McQueeney, Evolution of magnetic interactions in sb-substituted $mnbi_2te_4$, Phys. Rev. B **104**, 064401 (2021).

[20] C. Yan, S. Fernandez-Mulligan, R. Mei, S. H. Lee, N. Protic, R. Fukumori, B. Yan, C. Liu, Z. Mao, and S. Yang, Origins of electronic bands in the antiferromagnetic topological insulator $mnbi_2te_4$, Phys. Rev. B **104**, L041102 (2021).

[21] T. Fukasawa, S. Kusaka, K. Sumida, M. Hashizume, S. Ichinokura, Y. Takeda, S. Ideta, K. Tanaka, R. Shimizu, T. Hitosugi, and T. Hirahara, Absence of ferromagnetism in $MnBi_2Te_4/Bi_2Te_3$ down to 6 k, Phys. Rev. B **103**, 205405 (2021).

[22] B. Xu, Y. Zhang, E. H. Alizade, Z. A. Jahangirli, F. Lyzwa, E. Sheveleva, P. Marsik, Y. K. Li, Y. G. Yao, Z. W. Wang, B. Shen, Y. M. Dai, V. Kataev, M. M. Otrokov, E. V. Chulkov, N. T. Mamedov, and C. Bernhard, Infrared study of the multiband low-energy excitations of the topological antiferromagnet $mnbi_2te_4$, Phys. Rev. B **103**, L121103 (2021).

[23] M. Sitte, A. Rosch, E. Altman, and L. Fritz, Topological Insulators in Magnetic Fields: Quantum Hall Effect and Edge Channels with a Nonquantized θ Term, Phys. Rev. Lett. **108**, 126807 (2012).

[24] F. Tang, Y. Ren, P. Wang, R. Zhong, J. Schneeloch, S. A. Yang, K. Yang, P. A. Lee, G. Gu, Z. Qiao, and L. Zhang, Three-dimensional quantum hall effect and metal–insulator transition in zrte5, Nature (London) **569**, 537 (2019).

[25] Y. Xu, I. Miotkowski, C. Liu, J. Tian, H. Nam, N. Alidoust, J. Hu, C.-K. Shih, M. Z. Hasan, and Y. P. Chen, Observation of topological surface state quantum hall effect in an intrinsic three-dimensional topological insulator, Nat. Phys. **10**, 956 (2014).

[26] T. Schumann, L. Galletti, D. A. Kealhofer, H. Kim, M. Goyal, and S. Stemmer, Observation of the Quantum Hall Effect in Confined Films of the Three-Dimensional Dirac Semimetal cd_3as_2, Phys. Rev. Lett. **120**, 016801 (2018).

[27] C. Zhang, Y. Zhang, X. Yuan, S. Lu, J. Zhang, A. Narayan, Y. Liu, H. Zhang, Z. Ni, R. Liu, E. S. Choi, A. Suslov, S. Sanvito, L. Pi, H.-Z. Lu, A. C. Potter, and F. Xiu, Quantum hall effect based on weyl orbits in cd3as2, Nature (London) **565**, 331 (2019).

[28] W. A. Benalcazar, B. A. Bernevig, and T. L. Hughes, Quantized electric multipole insulators, Science **357**, 61 (2017).

[29] W. A. Benalcazar, B. A. Bernevig, and T. L. Hughes, Electric multipole moments, topological multipole moment pumping, and chiral hinge states in crystalline insulators, Phys. Rev. B **96**, 245115 (2017).

[30] Z. Song, Z. Fang, and C. Fang, $(d-2)$-Dimensional Edge States of Rotation Symmetry Protected Topological States, Phys. Rev. Lett. **119**, 246402 (2017).

[31] J. Langbehn, Y. Peng, L. Trifunovic, F. von Oppen, and P. W. Brouwer, Reflection-Symmetric Second-Order Topological Insulators and Superconductors, Phys. Rev. Lett. **119**, 246401 (2017).

[32] M. Geier, L. Trifunovic, M. Hoskam, and P. W. Brouwer, Second-order topological insulators and superconductors with an order-two crystalline symmetry, Phys. Rev. B **97**, 205135 (2018).

[33] S. Imhof, C. Berger, F. Bayer, J. Brehm, L. W. Molenkamp, T. Kiessling, F. Schindler, C. H. Lee, M. Greiter, T. Neupert,

and R. Thomale, Topolectrical-circuit realization of topological corner modes, Nat. Phys. **14**, 925 (2018).

[34] F. Schindler, A. M. Cook, M. G. Vergniory, Z. Wang, S. S. P. Parkin, B. A. Bernevig, and T. Neupert, Higher-order topological insulators, Sci. Adv. **4**, eaat0346 (2018).

[35] L. Trifunovic and P. W. Brouwer, Higher-Order Bulk-Boundary Correspondence for Topological Crystalline Phases, Phys. Rev. X **9**, 011012 (2019).

[36] B. Fu, Z.-A. Hu, and S.-Q. Shen, Bulk-hinge correspondence and three-dimensional quantum anomalous hall effect in second-order topological insulators, Phys. Rev. Res. **3**, 033177 (2021).

[37] I. Petrides and O. Zilberberg, Higher-order topological insulators, topological pumps and the quantum hall effect in high dimensions, Phys. Rev. Res. **2**, 022049(R) (2020).

[38] Y. Volpez, D. Loss, and J. Klinovaja, Second-Order Topological Superconductivity in π-Junction Rashba Layers, Phys. Rev. Lett. **122**, 126402 (2019).

[39] K. Laubscher, D. Loss, and J. Klinovaja, Fractional topological superconductivity and parafermion corner states, Phys. Rev. Res. **1**, 032017(R) (2019).

[40] L. Fu, C. L. Kane, and E. J. Mele, Topological Insulators in Three Dimensions, Phys. Rev. Lett. **98**, 106803 (2007).

[41] S.-Y. Xu, M. Neupane, C. Liu, D. Zhang, A. Richardella, L. Andrew Wray, N. Alidoust, M. Leandersson, T. Balasubramanian, J. Sánchez-Barriga, O. Rader, G. Landolt, B. Slomski, J. Hugo Dil, J. Osterwalder, T.-R. Chang, H.-T. Jeng, H. Lin, A. Bansil, N. Samarth, and M. Zahid Hasan, Hedgehog spin texture and berry's phase tuning in a magnetic topological insulator, Nat. Phys. **8**, 616 (2012).

[42] E. D. L. Rienks, S. Wimmer, J. Sánchez-Barriga, O. Caha, P. S. Mandal, J. Růžička, A. Ney, H. Steiner, V. V. Volobuev, H. Groiss, M. Albu, G. Kothleitner, J. Michalička, S. A. Khan, J. Minár, H. Ebert, G. Bauer, F. Freyse, A. Varykhalov, O. Rader, and G. Springholz, Large magnetic gap at the dirac point in bi2te3/mnbi2te4 heterostructures, Nature (London) **576**, 423 (2019).

[43] E. Khalaf, Higher-order topological insulators and superconductors protected by inversion symmetry, Phys. Rev. B **97**, 205136 (2018).

[44] K. Plekhanov, M. Thakurathi, D. Loss, and J. Klinovaja, Floquet second-order topological superconductor driven via ferromagnetic resonance, Phys. Rev. Res. **1**, 032013(R) (2019).

[45] Y. Ren, Z. Qiao, and Q. Niu, Engineering Corner States from Two-Dimensional Topological Insulators, Phys. Rev. Lett. **124**, 166804 (2020).

[46] K. Laubscher, D. Chughtai, D. Loss, and J. Klinovaja, Kramers pairs of majorana corner states in a topological insulator bilayer, Phys. Rev. B **102**, 195401 (2020).

[47] K. Laubscher, D. Loss, and J. Klinovaja, Majorana and parafermion corner states from two coupled sheets of bilayer graphene, Phys. Rev. Res. **2**, 013330 (2020).

[48] K. Plekhanov, F. Ronetti, D. Loss, and J. Klinovaja, Hinge states in a system of coupled rashba layers, Phys. Rev. Res. **2**, 013083 (2020).

[49] K. Plekhanov, N. Müller, Y. Volpez, D. M. Kennes, H. Schoeller, D. Loss, and J. Klinovaja, Quadrupole spin polarization as signature of second-order topological superconductors, Phys. Rev. B **103**, L041401 (2021).

[50] R. Jackiw and C. Rebbi, Solitons with fermion number, Phys. Rev. D **13**, 3398 (1976).

[51] R. B. Laughlin, Quantized hall conductivity in two dimensions, Phys. Rev. B **23**, 5632 (1981).

[52] D. J. Thouless, M. Kohmoto, M. P. Nightingale, and M. den Nijs, Quantized Hall Conductance in a Two-Dimensional Periodic Potential, Phys. Rev. Lett. **49**, 405 (1982).

[53] J. E. Avron, R. Seiler, and B. Simon, Homotopy and Quantization in Condensed Matter Physics, Phys. Rev. Lett. **51**, 51 (1983).

[54] M. Kohmoto, Topological invariant and the quantization of the hall conductance, Ann. Phys. **160**, 343 (1985).

[55] J.-H. Park, G. Yang, J. Klinovaja, P. Stano, and D. Loss, Fractional boundary charges in quantum dot arrays with density modulation, Phys. Rev. B **94**, 075416 (2016).

[56] M. Thakurathi, J. Klinovaja, and D. Loss, From fractional boundary charges to quantized hall conductance, Phys. Rev. B **98**, 245404 (2018).

[57] M. Pletyukhov, D. M. Kennes, J. Klinovaja, D. Loss, and H. Schoeller, Surface charge theorem and topological constraints for edge states: Analytical study of one-dimensional nearest-neighbor tight-binding models, Phys. Rev. B **101**, 165304 (2020).

[58] M. Pletyukhov, D. M. Kennes, J. Klinovaja, D. Loss, and H. Schoeller, Topological invariants to characterize universality of boundary charge in one-dimensional insulators beyond symmetry constraints, Phys. Rev. B **101**, 161106(R) (2020).

[59] M. Pletyukhov, D. M. Kennes, K. Piasotski, J. Klinovaja, D. Loss, and H. Schoeller, Rational boundary charge in one-dimensional systems with interaction and disorder, Phys. Rev. Res. **2**, 033345 (2020).

[60] S. Miles, D. M. Kennes, H. Schoeller, and M. Pletyukhov, Universal properties of boundary and interface charges in continuum models of one-dimensional insulators, Phys. Rev. B **104**, 155409 (2021).

[61] N. Müller, K. Piasotski, D. M. Kennes, H. Schoeller, and M. Pletyukhov, Universal properties of boundary and interface charges in multichannel one-dimensional models without symmetry constraints, Phys. Rev. B **104**, 125447 (2021).

[62] K. Laubscher, C. S. Weber, D. M. Kennes, M. Pletyukhov, H. Schoeller, D. Loss, and J. Klinovaja, Fractional boundary charges with quantized slopes in interacting one- and two-dimensional systems, Phys. Rev. B **104**, 035432 (2021).

[63] C. S. Weber, K. Piasotski, M. Pletyukhov, J. Klinovaja, D. Loss, H. Schoeller, and D. M. Kennes, Universality of Boundary Charge Fluctuations, Phys. Rev. Lett. **126**, 016803 (2021).

[64] K. Piasotski, M. Pletyukhov, C. S. Weber, J. Klinovaja, D. M. Kennes, and H. Schoeller, Universality of abelian and non-abelian wannier functions in generalized one-dimensional aubry-andré-harper models, Phys. Rev. Res. **3**, 033167 (2021).

[65] A. L. C. Hayward, E. Bertok, U. Schneider, and F. Heidrich-Meisner, Effect of disorder on topological charge pumping in the rice-mele model, Phys. Rev. A **103**, 043310 (2021).

[66] http://scicore.unibas.ch/.

[67] S. Datta, *Electronic Transport in Mesoscopic Systems* (Cambridge University Press, Cambridge, 1995), pp. 141–145.

[68] S.-Q. Shen, *Topological Insulators: Dirac Equation in Condensed Matters*, 2nd ed. (Springer Nature, Singapore, 2017).

[69] P. Hosur, P. Ghaemi, R. S. K. Mong, and A. Vishwanath, Majorana Modes at the Ends of Superconductor Vortices in Doped Topological Insulators, Phys. Rev. Lett. **107**, 097001 (2011).

[70] V.-N. Do, Non-equilibrium green function method: Theory and application in simulation of nanometer electronic devices, Adv. Nat. Sci.: Nanosci. Nanotechnol. **5**, 033001 (2014).